Research Article

Air-gap-free epidermal bioelectronics via ethanol-triggered interfacial reconstruction for high-quality electrophysiological monitoring

Huijun Kong[1], Chenshu Wu[1], Cuiyu Liu[1], Weiyan Li[1], Li Niu[2,*], Zhongqian Song[1,*]

[1]School of Chemistry and Pharmaceutical Engineering, c/o College of Medical Information and Artificial Intelligence, Shandong First Medical University & Shandong Academy of Medical Sciences, Jinan 250117, Shandong, China.
[2]School of Chemical Engineering and Technology, Sun Yat-sen University, Zhuhai 519082, Guangdong, China.

Correspondence to: Prof. Zhongqian Song, College of Medical Information and Artificial Intelligence, Shandong First Medical University, Jinan 250117, Shandong, China. E-mail: zqsong@sdfmu.edu.cn; Prof. Li Niu, School of Chemical Engineering and Technology, Sun Yat-sen University, Zhuhai 519082, Guangdong, China. E-mail: niuli@mail.sysu.edu.cn

How to cite this article: Kong, H.; Wu, C.; Liu, C.; Li, W.; Niu, L.; Song, Z. Air-gap-free epidermal bioelectronics via ethanol-triggered interfacial reconstruction for high-quality electrophysiological monitoring. *Soft Sci.* 2026;6:[Accepted]. https://dx.doi.org/10.20517/ss.2026.51

Received: 12 March 2026 | **Revised:** 27 May 2026 | **Accepted:** 28 May 2026

Abstract

Stable and high-fidelity electrophysiological monitoring with dry epidermal electrodes remains limited by interfacial air gaps and mechanical mismatch, which induce dynamic impedance fluctuations and severe motion artifacts during skin deformation. Here, we introduce an ethanol-triggered interfacial reconstruction strategy that directly fabricates a ~ 5 μm-thick conductive nanomesh onto the epidermis, seamlessly conforming to complex skin micro-textures. This interfacial reconstruction effectively eliminates trapped air gaps, reduces mechanical mismatch, and establishes a stable low-impedance

bioelectronic interface (37.8 kΩ at 100 Hz). Thus, it enables high-quality electrophysiological recordings with higher signal-to-noise ratio compared to commercial gel electrodes. The resulting nanomesh electrode exhibits high breathability and conformality, robust resistance to sweat, and on-demand ethanol-assisted removability. Hence, it allows long-term, irritation-free monitoring of electrophysiological signals under dynamic deformation and wet conditions. This thin epidermal electrode provides a new pathway toward reliable acquisition of electrophysiological signals, offering broad potential for personalized health monitoring, early disease diagnosis, and next-generation brain-computer interfaces.

Keywords: Air-gap-free interface, conformal electrode, low-motion artifact, electrophysiological recording

INTRODUCTION

Electrophysiological signals originate from the electrical activity of excitable cells during physiological processes. The main types include electromyography (EMG) generated by muscle action, electrocardiography (ECG) from cardiac beating, electroencephalography (EEG) produced by brain electrical activity, and electrooculography (EOG) from eyeball or eyelid movements[1-4]. Skin-mounted epidermal electronics can continuously collect physiological information, creating an opportunity for personalized health monitoring, human-machine collaboration, and precise disease diagnosis[5-8]. A stable electronic-skin interface is crucial to ensure low interfacial impedance and accurate signal acquisition[9-12]. However, dynamic skin activities might introduce mechanical disturbances and detachment or displacement of electrodes, thereby causing signal distortion and low reliability in electrophysiological measurements[13-15]. Establishing a stable, low-impedance, and motion-artifact-resistant electrode-skin interface is a prerequisite for achieving high-quality electrophysiological recording.

Commercial gel-type and conductive hydrogel-based electrophysiological electrodes can form seamless contact with skin due to the mechanical softness and tunable adhesiveness, achieving low interfacial impedance and high signal-to-noise ratio (SNR)[16-23]. However, hydrogels dehydrate in open air, leading to increased contact impedance and a shorter lifetime. Moreover, prolonged hydrogel use may induce skin irritation or allergic reactions[10, 24-26]. In contrast, dry epidermal electrodes, including metallic films[27,28],

carbon materials[29-32] and conductive polymers[33-36], establish direct skin contact, offering simplicity, long-term usability, and easy system integration[34,37-39].

Extensive research has focused on engineering conformable and stable electrode-skin interfaces to mitigate skin deformation artifacts. However, complex curvilinear skin surfaces often create air gaps at the electrode-skin interface, reducing contact area and increasing interfacial impedance. During natural skin deformation, such as stretching, compression, and torsion, the air gaps could result in interfacial delamination and severe motion artifacts that distort electrophysiological signals[37,40]. Various strategies, such as reducing electrode thickness, lowering elastic modulus, or enhancing adhesion, could promote compliance with the skin. However, the solid-to-solid contact cannot completely eliminate interfacial air gaps due to the micro-concave features of skin surface[41,42]. Interface engineering strategies, such as capillary-driven transfer[41] and interfacial-controllable dissolution[43], could eliminate air gaps, enabling seamless contact with the wrinkled skin surface. Moreover, strong adhesion may hinder painless removal, and breathable structures may compromise interfacial electrical stability[44]. Therefore, achieving an air-gap-free, mechanically stable, and skin-friendly bioelectronic interface remains an unresolved challenge for dry epidermal electrophysiology.

Here, we introduce an ethanol-triggered interfacial reconstruction strategy that enables the in situ formation of air-gap-free epidermal bioelectronics directly on the skin surface. Unlike conventional attachment-based approaches, this strategy reconstructs the electrode-skin interface during the transfer process. Benefiting from the selective solubility of sacrificial polymer nanofibers in ethanol, a conductive nanomesh is reconstructed on the epidermis, allowing seamless conformability to complex skin micro-textures. This reconstruction process effectively eliminates trapped air gaps and establishes a continuous and stable bioelectronic interface with low-contact impedance (37.8 kΩ at 100 Hz). The reconstructed nanomesh electrode exhibits desirable properties essential for electrophysiological monitoring, including low thickness (5 μm), high water-vapor transmission rate (60 g m^{-2} h^{-1}), resistance to sweat, and on-demand ethanol-assisted removability. These characteristics enable long-term, irritation-free wear and stable interfacial impedance under dynamic skin deformation. Consequently, the electrode achieves high-quality electrophysiological recordings with suppressed motion

artifacts and reliable acquisition of EMG, ECG, EOG, and EEG signals. The ethanol-triggered reconstruction strategy offers a new pathway toward skin-integrated bioelectronics, opening new opportunities for personalized health monitoring, early disease diagnosis, and next-generation brain-computer interfaces.

EXPERIMENTAL

Materials

Poly(vinyl butyral) (PVB) powder, with a molecular weight of 90,000 ~ 120,000 was obtained from Shanghai Macklin Biochemical Co., Ltd, China. Silver nanowires (AgNWs) dispersion in ethanol (10 mg/mL) was purchased from Jilin 11 Technology Co., Ltd., China, and diluted to the target concentration for use. Glycerol, ethanol, and N, N-dimethylformamide were purchased from Shanghai Macklin Biochemical Co., Ltd., China. Acrylic pressure-sensitive medical adhesive (DURO-TAK 180-129A) was supplied by Henkel (China) Investment Co., Ltd. Human embryonic kidney 293T cells were purchased from Procell Life Science & Technology Co., Ltd. (Wuhan). All reagents were used without further purification.

Preparation of nanomesh electrode

The PVB nanomesh electrode was fabricated by electrospinning method. Specifically, 1.4 g of PVB powder was dissolved in 18.6 g of mixed solvent (N, N-dimethylformamide and ethanol, with a mass ratio of 1:2) and stirred at 600 rpm (25 ℃) for 12 h to obtain a 7 wt.% solution. The solution was then loaded in a syringe equipped with a 20-gauge-diameter metallic needle. The electrospinning process was conducted using a commercial electrospinning apparatus under following conditions: an applied voltage of 25 kV, a solution flow rate of 0.8 ml/h, and a working distance of 10 cm between the needle tip and collector. The PVB nanofiber membrane was acquired after electrospinning for 1.5 h. A gold layer was sputtered onto PVB nanofiber via magnetron sputtering (HeZao GMC-1000, Shanghai) at a deposition current of 40 mA, and the thickness of gold was adjusted by varying the deposition time. The PVB nanomesh electrode was then peeled off from substrate for further usage.

Transfer process of nanomesh electrode onto human skin

A 10 wt.% solution of the medical adhesive (MA) was prepared by dissolving MA in ethanol. The silver nanowire (AgNWs)/ethanol solution was then diluted to the target

concentrations of 0.1, 1, and 2 mg/mL. Subsequently, MA and glycerol were added to the Ag NWs/ethanol solution (1 ml) with optimized amounts (0.05 g of MA and 0.2 g of glycerol), yielding the final Gly/Ag NWs/MA/ethanol transfer solution. In the following transfer process, skin surface of human subjects was first cleaned with 75% ethanol to remove dirt. Gly/Ag NWs/MA/ethanol solution was then applied onto the bare skin, after which the PVB nanomesh electrodes with rectangular shape (1 cm × 1 cm) were carefully positioned onto the wetted region without external pressure. After 1 min of ethanol evaporation, the nanomesh electrode adhered tightly and seamlessly to the skin surface. The transferred PVB nanomesh electrodes were prepared for the following electrical measurement.

Characterization

Surface and cross-sectional images of the nanomesh electrode were characterized by scanning electron microscope (Hitachi Regulus 8100, Japan) at an acceleration voltage of 5 kV; EDS mapping was performed at 10 kV. Fourier Transform Infrared Spectroscopy (FTIR) analysis was conducted by Thermo Fisher Scientific Nicolet iS20, USA. Optical images were obtained using an optical microscope (GP-660V, China). Contact angles of nanomesh electrode with water or ethanol medium were characterized using an optical contact angle meter (JY-82C, Dingsheng, China) equipped with a CCD camera (UA5MAGCXP-111M/C, China). Infrared images of the skin were acquired using an infrared camera (HIKMICRO, H16, China). The mechanical properties of the PVB nanofibers were evaluated using a tensile testing system (BWN-100N, Beiguang Jingyi Instrument, China). The electrical resistance of the electrode was acquired from a digital source meter (Keithley 2450, Tektronix, America). The contact impedance of the electrode-skin interface was characterized with an LCR meter (TH2840A, Tonghui, China), with frequencies ranging from 500 kHz to 20 Hz.

Electrophysiological recording

The electrophysiological signals were captured by a signal acquisition and processing system (BL-420N, TaiMeng, China). All electrophysiological measurements were performed on the skin of human volunteers ($n = 3$) in accordance with institutional ethical standards and with the consent of all participants. Each experiment was repeated at least three times to ensure reproducibility. To capture EMG signals, two nanomesh electrodes with a rectangular shape (1 cm × 1 cm) were adhered onto forearm flexor muscles as

recording electrodes, while a commercial Ag/AgCl electrode was attached to the elbow as a ground electrode. All EMG data were filtered using a 2 kHz low-pass filter. For ECG recording, two measurement electrodes were mounted on the left arm (LA) and right leg (RL), and the ground electrode was attached onto right arm (RA). The SNR of the electrophysiological electrode was calculated as:

$$SNR = 20log\frac{V_{RMS,signal}}{V_{RMS,noise}}$$

where $V_{RMS,signal}$ denotes the RMS values of signals, and $V_{RMS,noise}$ denotes the RMS values of the noise.

For EOG signal measurement, two recording nanomesh electrodes (1 cm × 1 cm) were placed above the volunteer's eyebrow and the lower orbital edge, respectively. Another electrode was attached onto the postauricular bone as ground electrode. The signals were captured when the volunteer move eyeballs or eyelids. In the EEG measurement, nanomesh electrodes were attached onto the right mastoid as reference electrode and the right forehead as recording electrode, while another nanomesh electrode was positioned onto the left mastoid as ground electrode.

RESULTS AND DISCUSSION

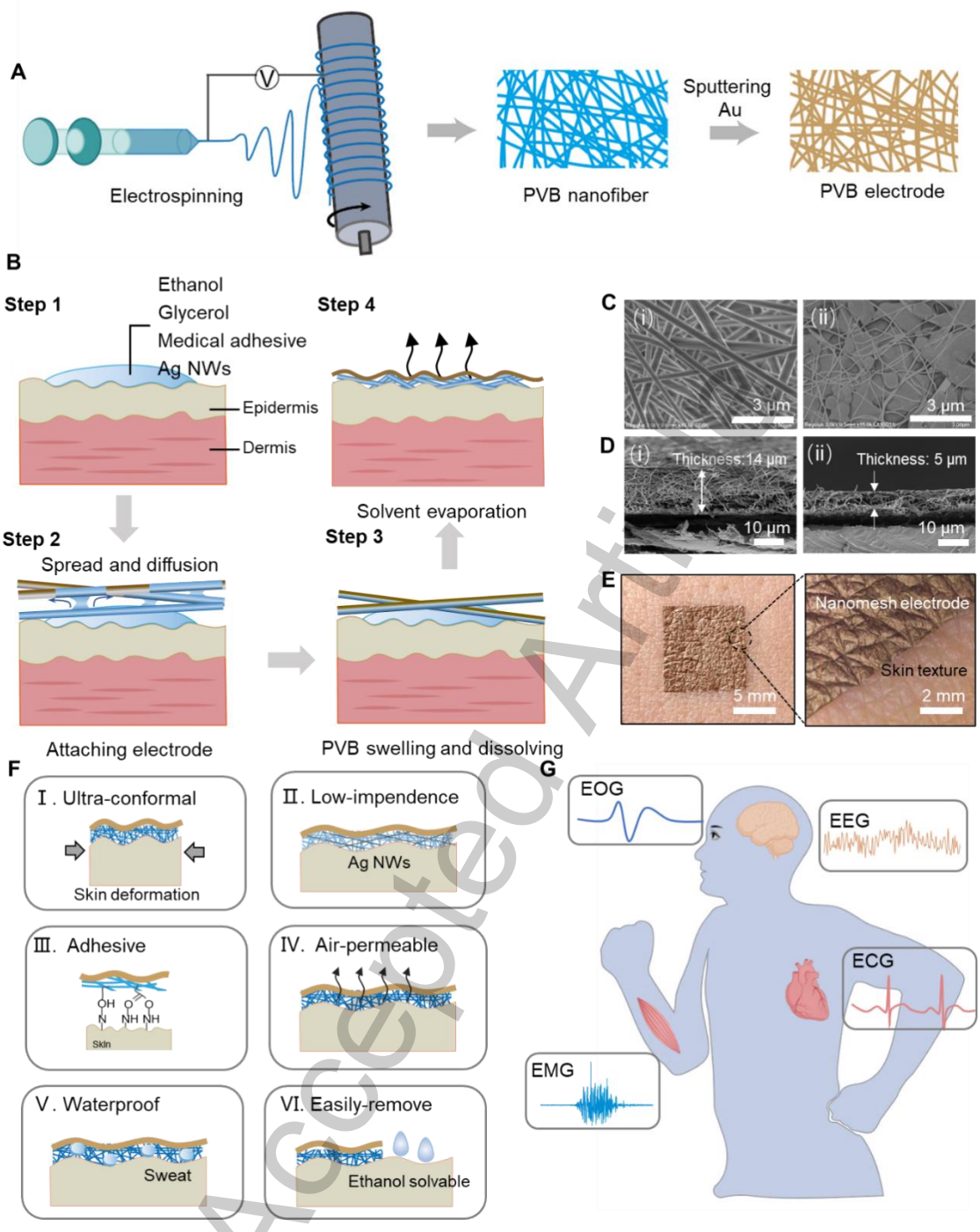

Figure 1. (A) Schematic illustration of the fabrication process of the sacrificial PVB nanofiber-based nanomesh electrode. (B) Schematic illustration of the ethanol-triggered in-situ interfacial reconstruction process on human skin, including wetting, capillary infiltration, nanofiber dissolution, and interface reconstruction, leading to an air-gap-free and conformal epidermal electrode. (C) Surface and (D) cross-sectional morphology of nanomesh electrode before and after the interfacial reconstruction process. (E) Photograph of the nanomesh electrode reconstructed directly on human skin, and the enlarged view of the boundary between skin and nanomesh electrode. (F) Summary of

key performance metrics of the nanomesh electrode, including conformality, low interfacial impedance, strong adhesion, high breathability, water resistance, and ethanol-assisted removability. (G) Illustration of the conformal electrode for continuous biopotential signal measurement.

Ethanol-triggered interfacial reconstruction of an air-gap-free nanomesh electrode for epidermal electrophysiology

To overcome the air gap-induced unstable contact of electrode-skin interface, a sacrificial nanofiber-based transfer strategy is introduced to construct seamless contact. Sacrificial nanofiber was prepared by electrospinning PVB solution to form a mesh-like nanofiber layer, and subsequently treated with magnetron sputtering to fabricate the nanomesh electrode [Figure 1A]. The density of microfiber network is influenced by electrospinning time [Supplementary Figure 1].

The total energy of electrode-skin interface (U_{total}) was expressed as[37]:

$$U_{total} = U_{bending} + U_{skin} + U_{adhesion} + U_{membrane}$$

where $U_{bending}$ denotes bending energy of the interface system, U_{skin} denotes skin elastic energy, $U_{adhesion}$ denotes adhesion energy of interface, and $U_{membrane}$ denotes membrane energy. To ensure conformal contact between electrode and skin, U_{total} should be minimized. Hence, MA was supplemented to the transfer solution to enhance adhesiveness and lower $U_{adhesion}$, while glycerol (Gly) was employed as plasticizer for the nanomesh electrode, thereby reducing $U_{bending}$ and $U_{membrane}$. In addition, AgNWs were supplemented to reduce the interfacial contact impedance. Consequently, the Gly/AgNWs/MA/ethanol quaternary solution was prepared with optimized concentration for usage.

The Gly/AgNWs/MA/ethanol transfer solution was then applied to the skin, where it spread over the skin surface due to the low surface tension of ethanol, as illustrated in step 1 of Figure 1B[45]. In step 2, the PVB nanomesh electrode was placed onto the wetted region. The pores between the nanofibers rapidly absorbed the transfer solution via capillary forces, promoting horizontal liquid spreading. Excessive accumulation of solution enabled liquid contact with the upper layer, forming a liquid bridge that transported the solution to the next layer. Consequently, the bottom nanofibers underwent

swelling and dissolving process (Step 3) and created an ultrathin fluid layer that perfectly conformed to skin topography. The upper layer retained the fibrous structure due to the lack of contact with transfer solution. As the ethanol in the solution evaporated, a conformal electrode was formed in situ on the skin without air gaps (Step 4), while the hydrogen bonds formed at the electrode-skin interface facilitated a self-adhesion process. The detailed transfer procedure is shown in Supplementary Movie 1. The ethanol-triggered transfer process effectively eliminated the air gaps at the electrode-skin interface, allowing seamless conformability to the microstructured substrate [Supplementary Figure 2]. This physical dissolution-reconstruction process ensures stable electrical coupling and preserves the flexibility of the electrode for subsequent electrophysiological measurements. The surface morphology of the nanomesh electrode in Figure 1C(i) and (ii) indicates that the fibrous structure transformed into a dense structure after the in situ dissolving-adhesion process. In addition, the energy dispersive spectroscopy (EDS) analysis of the bottom surface after transfer [Supplementary Figure 3] confirms that interwoven silver nanowires were embedded into PVB matrix, which contributed to the low contact impedance and high SNR of the nanomesh electrode. Cross-sectional images of the nanomesh electrode revealed that the thickness decreased from 14 μm to 5 μm after the transfer process [Figure 1D], indicating the dissolution of underlying PVB nanomesh. The upper layer retained the fibrous structures, which endowed the nanomesh electrode with excellent air permeability. The nanomesh electrode was transferred on the back of the hand [Figure 1E], and the enlarged image exhibited ultrahigh conformality to skin textures. The sheet resistance displays negligible variation after the transfer process, confirming the non-destructive transfer of this sacrificial nanofiber-based method [Supplementary Figure 4].

Consequently, as illustrated in Figure 1F, the nanomesh electrode could maintain a seamless, conformal interface with skin during dynamic movements. This performance could be attributed to the air-gap-free interface, low thickness, strong adhesion, and mechanical softness. The embedded AgNWs could reduce contact impedance, thereby delivering high-quality signals and accurate monitoring. The adhesiveness is ascribed to hydrogen bonds formed at the interface, while the air permeability is linked to porous microstructure. Moreover, the dissolvable nature of PVB provides waterproof properties and enables facile removal with ethanol, ensuring user comfort during practical use. Hence, the nanomesh-based electrode demonstrates unparalleled advantages for high-

quality electrophysiological recording (including EMG, EOG, ECG, and EEG), as shown in Figure 1G, demonstrating broad application potential in human-machine interfaces, cardiac status evaluation, and clinical diagnosis.

Interfacial and mechanical stability, breathability, and compatibility of the air-gap-free nanomesh electrode

Air gaps usually exist between conventional dry electrodes and the skin interface (Figure 2A, top), which may compromise mechanical stability and result in micro-delamination when the skin is subjected to repetitive stretching or compression. In contrast, the nanomesh electrode could maintain conformality under dynamic skin deformation (Figure 2A, bottom), which is ascribed to two key factors. First, the in situ dissolving-adhesion process effectively eliminated interfacial air gaps, thereby mitigating mechanical instability at the electrode-skin interface. Second, Gly/Ag NW/MA/ethanol transfer solution was specifically formulated to improve stretchability and adhesion, enabling the electrode to conform seamlessly under dynamic skin movements. To investigate compliance with human skin, the nanomesh electrode was transferred onto the back of hand using a Gly/Ag NW/MA/ethanol solution. The photographs of the nanomesh electrode with undeformed, stretching, compressing and twisting deformation are shown in Figure 2B, indicating its ultimate adaptation with skin texture.

As aforementioned, the Gly/Ag NW/MA/ethanol transfer solution plays a pivotal role in enhancing stretchability and adhesion of the nanomesh electrode. Based on the theory of contact stability, the nanomesh electrode possesses low elastic modulus and strong adhesion, and can maintain conformal contact for a longer duration during skin deformation. Glycerol was employed as a plasticizer to enhance the softness of the nanofibers, and the tensile test results presented in Supplementary Figure 5 indicate that incorporation of glycerol promoted stretchability. The amounts of MA and glycerol can influence adhesion and compliance of nanomesh electrode-skin interface. Inadequate addition of MA could result in electrode detachment and unstable interface [Supplementary Figure 6A]. Insufficient glycerol can cause electrode cracks under skin deformation, while excessive Gly results in decrease of interfacial adhesion [Supplementary Figure 6B] and electrode detachment. The nanomesh electrode transferred onto a PET substrate exhibited excellent long-term electrical stability, and the resistance remained essentially unchanged over bending curvatures of 0-500 m^{-1} [Figure

2C]. Moreover, the nanomesh electrode exhibited negligible resistance variation under repeated bending tests (with bending curvatures of 500 m^{-1}), revealing the mechanical robustness and electrical stability under dynamic movements [Figure 2D]. The mechanical and electrical properties of the nanomesh electrode were characterized to assess the suitability for practical applications [Supplementary Figure 7]. The electrical resistance exhibited a gradual increase under applied strain of 30%, exceeding the typical human skin strain range of 20%-25%. Furthermore, the transferred nanomesh electrode could withstand 50% strain deformation without failure, ensuring the suitability at unexpected mechanical deformations.

Sweating and moisture are inevitable during long-term measurements, which may result in detachment and degradation of electrophysiological electrodes. The nanomesh electrode displayed a static water contact angle of 139.6°, due to the high surface free energy and rough microstructures (Supplementary Figure 8, left). When a water drop was placed on the nanomesh electrode transferred onto skin, the optical photograph confirmed its waterproof nature. After removing the water, the nanomesh electrode exhibited no discernible damage [Supplementary Figure 9A and B]. In contrast, the nanomesh electrode showed excellent affinity for ethanol, with a contact angle of 15.4°, due to the low surface tension [Supplementary Figure 8, right]. This facilitated the rapid spreading of ethanol during the transfer process. Leveraging its ethanol affinity and solubility, the PVB nanomesh electrode could be easily removed from the adhesive area using ethanol, without causing secondary skin damage. No characteristic absorption peaks of PVB were detected after ethanol-assisted removal, confirming the absence of detectable residue [Supplementary Figure 10]. Consequently, the electrode combined water-resistance with removal simplicity by ethanol [Supplementary Movie 2 and Figure 2E], which greatly enhanced its practicality in realistic applications.

The nanomesh electrode exhibited excellent air permeability due to the nanofiber-based porous architecture with low thickness. The water-vapor permeability of the nanomesh electrode was evaluated at 35℃ to simulate sweaty conditions. To highlight the advantages of the nanomesh electrode in air permeability, water vapor transmission rate (WVTR) of commonly used wearable materials was tested for comparison. As shown in Figure 2F and G, the nanomesh electrode exhibited markedly higher breathability (with WVTR of 60 g m^{-2} h^{-1}) than commercial gel electrode, PDMS substrate, and medical

tape. As a result, after a 24 h of skin attachment, the nanomesh electrode caused negligible redness and irritation compared with commercial gel electrode [Supplementary Figure 11]. Infrared thermography further revealed the temperature distribution between the electrode-amounted area and bare skin [Figure 2H]. Compared with commercial Ag/AgCl gel electrode, the PVB nanomesh exhibited no significant temperature difference with skin surface, where the low temperature of nanomesh electrode area was caused by low infrared emissivity of the metal. Furthermore, the biocompatibility of nanomesh electrode was evaluated through cytotoxicity assessments. Human embryonic kidney 293T cells were used to evaluate the influence of the electrodes on cell viability and proliferation. Confocal microscopy images [Figure 2I] displayed strong and homogenous fluorescence in 293T cells treated with PVB nanofiber and transferred nanomesh electrode, which was consistent with control group. The OD values increased with prolonged culture for all three groups, confirming the excellent biocompatibility of the nanomesh electrode [Figure 2J].

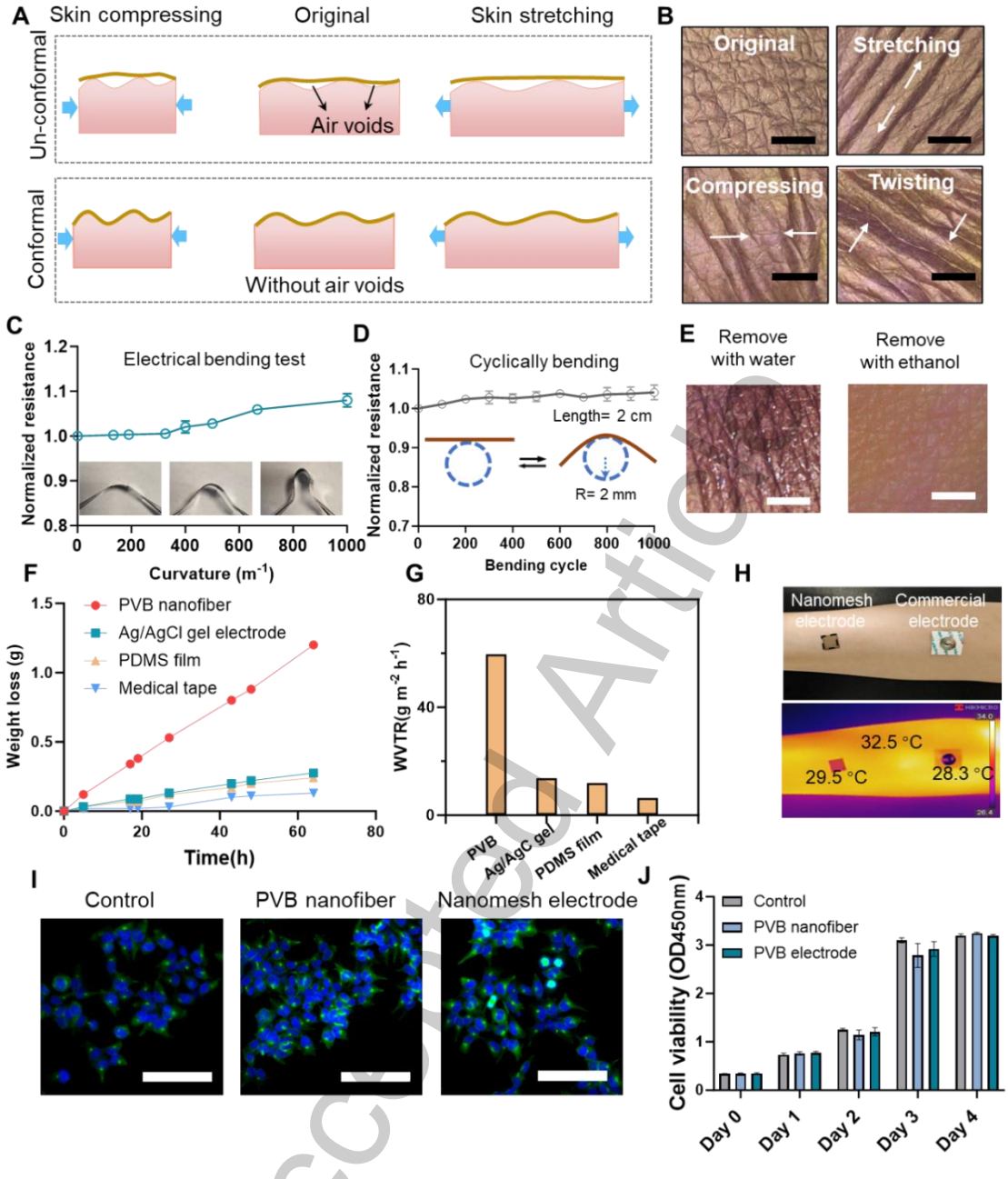

Figure 2. (A) Schematic comparison between a conventional dry electrode and the conformal nanomesh electrode at the electrode-skin interface under skin deformation. (B) Photographs of the nanomesh electrode subjected to undeformed, stretching, compressing and twisting deformation (scale bar: 2 mm). (C) Normalized resistance variation of the nanomesh electrode as a function of bending curvature of 0-1000 m^{-1}. (D) Resistance variation of the nanomesh electrode during 1000 bending cycles. (E) Photograph of the nanomesh electrode after removing with water or ethanol. Scale bar: 2 mm. (F) Water permeability curves of the nanomesh electrode under 35 ℃ conditions compared with Ag/AgCl gel electrode, PDMS film and medical tape, and (G)

corresponding water vapor transmission rate (WVTR). (H) Optical and infrared thermal images of the nanomesh and Ag/AgCl gel electrode attached onto human forearm. (I) Fluorescence microscopy images of 293T cells cultured with PVB nanofiber network and transferred nanomesh electrode. Scale bar: 100 μm. (J) Cell viability of 293T cells cultured with PVB nanofibers, transferred nanomesh electrode and a blank control. The results in C, D, and J are presented as mean ± standard deviation (C,D: n=3, J: n=6).

Electrical performance and motion-robust EMG recording of the nanomesh electrode

The nanomesh electrode in situ forms a seamless and conformal contact with the skin texture, minimizing air gaps at the interface and ensuring efficient electrophysiological signal transmission. The effects of transfer solution components on electrical performance were systematically investigated. First, the embedded AgNWs facilitated effective electrical contact between the electrode and the skin, thereby reducing the interfacial impedance and enabling high-quality monitoring. For electrical characterization, the cross-sectional resistance of nanomesh electrodes transferred with AgNWs solutions at different concentrations (0, 0.1, 1, and 2 mg/mL) is presented in Supplementary Figure 12. The nanomesh is essentially insulating in cross-section when transferred without AgNWs, whereas conductivity increases markedly with rising Ag content. The nanomesh electrodes were then transferred onto a volunteer's forearm for interface-impedance measurement. To clarify the charge-transport mechanism, the equivalent circuit of the electrode–skin interface is illustrated in Supplementary Figure 13. With increasing silver content, the contact impedance gradually reduces [Figure 3A]. At an AgNWs concentration of 2 mg/mL, the impedance of nanomesh electrode (37.8 kΩ at 100 Hz) is approximately 73 % lower than that of the commercial gel electrode (137 kΩ). Secondly, the effects of MA and Gly amounts on contact impedance are summarized in Supplementary Figure 14 A and B, indicating that excessive Gly could lead to increased impedance due to partial isolation of conductive pathways. In addition, the electrical performance of PVB nanomesh with various gold sputtering times (30, 60, 90 s) are evaluated in Supplementary Figure 15, indicating an optimized sputtering time of 90 s for signal acquisition.

Benefiting from the low interfacial impedance and highly conformal contact, the nanomesh electrode exhibits unparalleled advantages in high-quality EMG signals

measurement. Two nanomesh electrodes were attached to the forearm flexor muscles as recording electrodes, while a commercial electrode serves as ground electrode on the elbow [Figure 3B]. During the grip tests, the nanomesh electrode not only represents similar waveform characteristics as commercial gel electrode, but also delivers higher signal amplitude and an SNR of 42 dB, which remarkably exceeds the 34 dB SNR obtained with the commercial gel electrode [Figure 3C]. In addition, the nanomesh electrode can distinguish various muscle movements, as shown in Supplementary Figure 16. Based on the waterproof property of the nanomesh electrode, the electrical performances under wet conditions are characterized. The interfacial impedance variation curve during the hydrous experiment is shown in Supplementary Figure 17, indicating a slight decrease with the addition of water. The contact impedance variation curves across different frequencies in Figure 3D reveal that the electrical performance is almost unaffected by humid conditions. Moreover, the EMG signals recorded in the presence of water show negligible amplitude loss and no significant increase in noise [Figure 3E], indicating the electrical stability in sweaty or humid environments. To further evaluate performance under sweaty conditions, artificial sweat was applied to the nanomesh electrode. The contact impedance exhibited a decrease at low frequencies in sweaty state [Supplementary Figure 18], which could be attributed to enhanced ionic conductivity from the artificial sweat. The microscopic photographs under various deformations (original, stretching, compressing, and twisting deformations) are shown in Supplementary Figure 19, confirming the dynamic conformality and sweat resistance of the electrode.

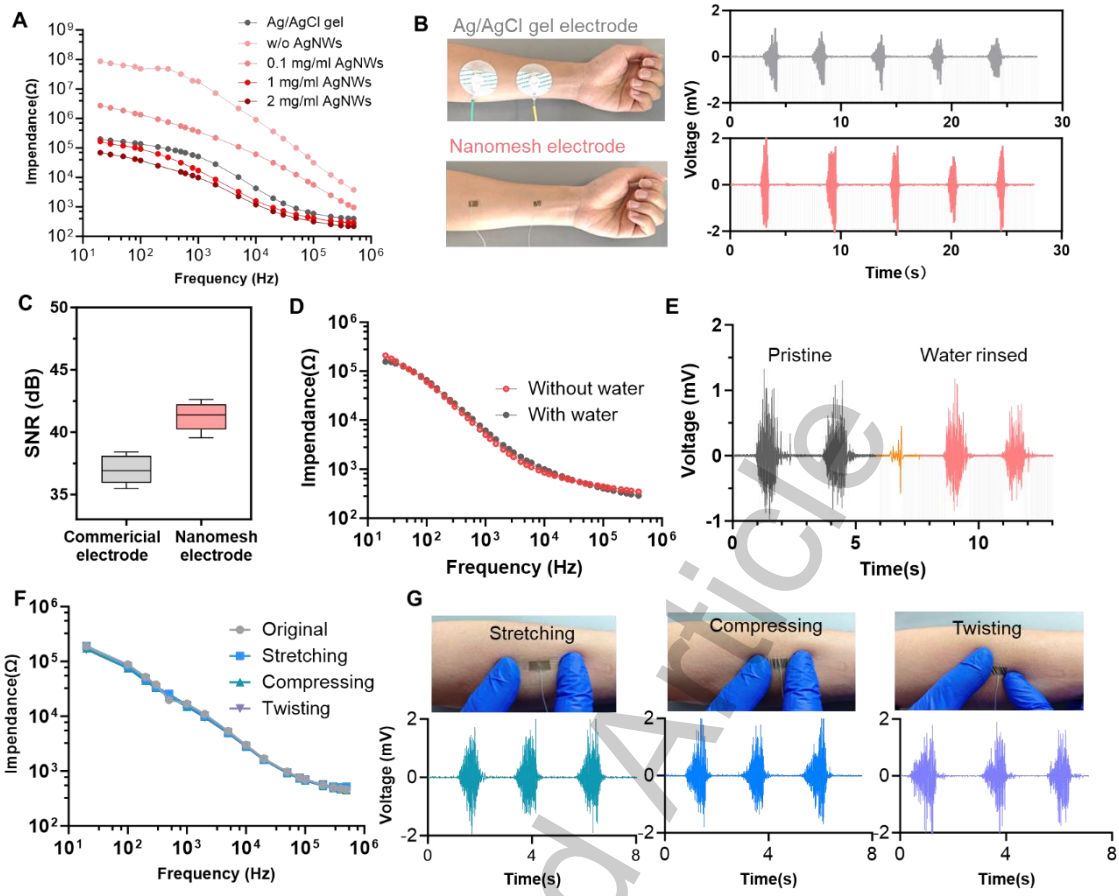

Figure 3. Electrical performance and motion-robust EMG recording of the nanomesh electrode. (A) Interfacial impedance of commercial Ag/AgCl gel electrode and nanomesh electrode transferred with AgNWs of various concentrations. (B) Photographs of EMG measurement and corresponding EMG signals acquired from Ag/AgCl gel electrode and nanomesh electrode during a hand-gripping action. (C) SNR of EMG signals acquired by the commercial electrode and nanomesh electrode. The results are presented as mean ± standard deviation (n=3). (D) Interfacial impedance and (E) recorded EMG signals of the nanomesh electrode measured under initial dry conditions and water-containing state. (F) Interfacial impedance and (G) EMG signals under undeformed, stretching, compressing, and twisting deformation.

Human physiological activities inevitably cause artifacts due to the instability at the electrode-skin interface, which may further induce signal baseline drift and severe signal distortion. As previously mentioned, our nanomesh electrode maintains good contact with irregularly curvilinear and dynamically changing skin surfaces due to its seamless interface, strong adhesiveness, and elasticity. Consequently, the nanomesh electrode

exhibits interface-impedance stability even under stretching, compressing, and twisting deformation, as shown in Figure 3F. Figure 3G shows that EMG signals can be reliably recorded even when the skin is stretched, compressed, or twisted, indicating that the nanomesh electrode exhibits excellent resistance to motion-artifact interference. For comparison, EMG signals captured by Ag/AgCl gel electrode with skin stretching, compressing, or twisting are recorded in Supplementary Figure 20. The commercial gel electrode exhibits a higher noise level under skin deformation, which is attributed to its unstable bioelectronic interface. Compared with commercial gel electrodes, the nanomesh electrodes exhibit higher SNR even under skin deformation [Supplementary Figure 21], indicating resistance to motion artifacts. Comparison of the nanomesh electrodes with other material-based epidermal electrodes highlights their superior performance, including reduced thickness, enhanced WVTR, lower interfacial contact impedance, higher SNR for electrophysiological recordings, and operational stability under wet and deforming conditions [Supplementary Table 1].

The ethanol-triggered reconstruction process is critical for ensuring interfacial stability and dynamic conformality of electrodes. The absence of MA in the transfer solution resulted in electrode detachment and formation of air voids during dynamic skin deformations, thereby increasing contact impedance at low frequencies [Supplementary Figure 22] and reduced signal amplitudes for EMG measurement [Supplementary Figure 23]. Without the ethanol transfer process, the PVB nanofiber layer functioned as an insulating barrier between the electrode and the skin, leading to significantly increased contact impedance and failure acquisition of EMG signals [Supplementary Figure 24A and B]. Therefore, the ethanol-assisted reconstruction process is indispensable for establishing a stable, low-impedance electrode-skin interface for long-term utilization. To evaluate long-term interfacial stability, the electrode-skin impedance was measured after 0, 6, and 12 h of continuous attachment [Supplementary Figure 25]. The slight variation in impedance indicates stable adhesion during prolonged skin wear.

High-quality ECG monitoring using the air-gap-free nanomesh electrode

A three-electrode system was constructed to monitor the ECG signals under static and dynamic conditions. As shown in Figure 4A, two nanomesh electrodes were attached onto the left arm (LA) and right leg (RL) as recording electrodes, while another nanomesh electrode was placed on the right arm (RA) as the ground electrode. Under

static conditions, the signals acquired from nanomesh electrodes exhibit strong morphological consistency with the commercial gel electrode, demonstrating effective capture of ECG waveform features, including the P wave, QRS complex, and T wave [Figure 4B]. The scatter plot of the R-R intervals is depicted in Supplementary Figure 26, indicating the potential applications in heart rate variability analysis.

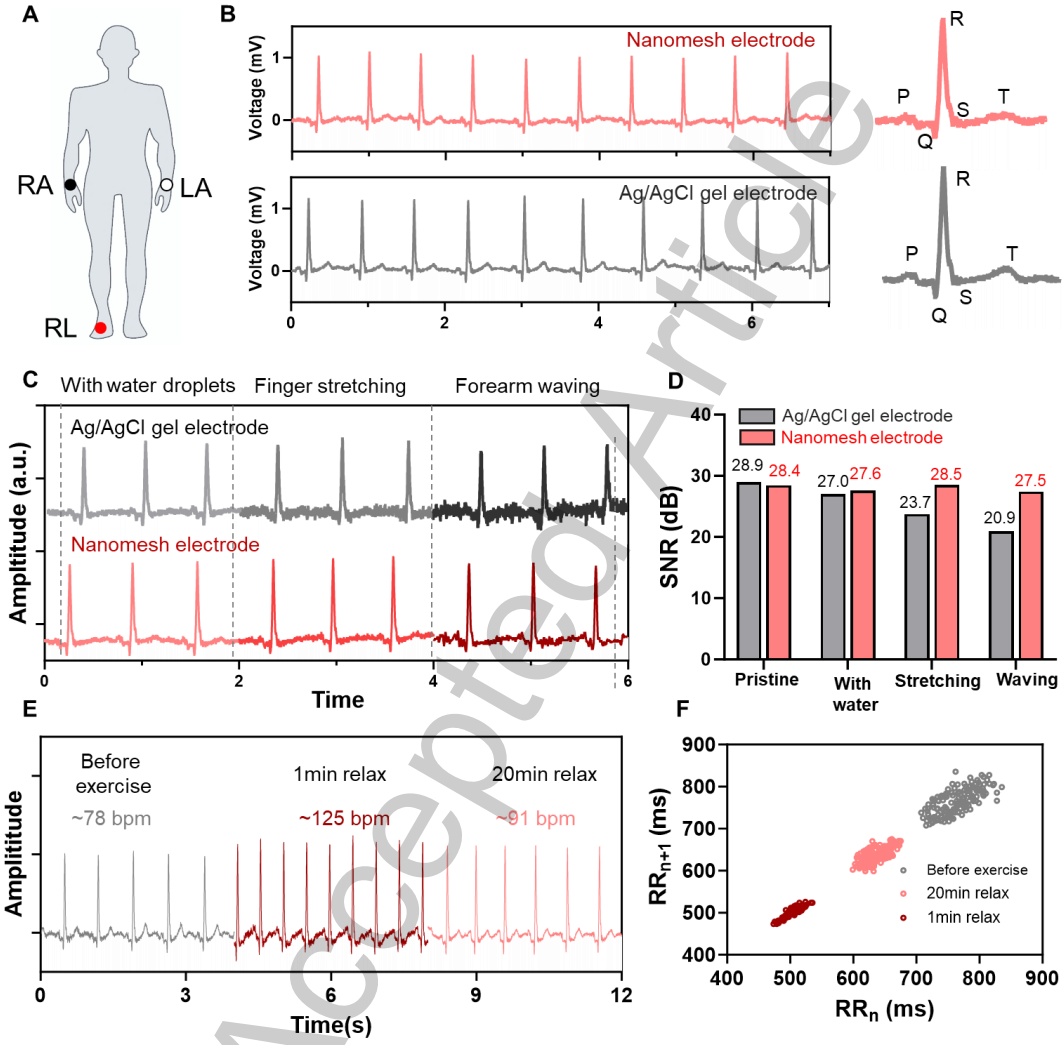

Figure 4. ECG measurement for low-motion artifacts by the nanomesh electrode under variable conditions. (A) Schematic illustration of the three-electrode configuration for ECG measurement, with nanomesh electrodes positioned on the left arm (LA) and right leg (RL) as recording electrodes and on the right arm (RA) as the ground electrode. (B) Comparative ECG signals recorded by nanomesh electrode (red) and commercial gel electrode (black) at rest state. (C) ECG signals measured by nanomesh electrode under various conditions, including wet, skin stretching, and forearm waving action. (D) Corresponding SNR values of ECG signals under various conditions. (E) Comparison of

ECG signals before and after 20-min exercise. (F) Scatter plot of R-R intervals derived from ECG signals before and after exercise.

Furthermore, to evaluate the monitoring accuracy of electrodes, the ECG signals were recorded under varying intricate conditions, including wet, stretched, and forearm waving movements [Figure 4C]. The commercial gel electrode exhibits relatively reliable waveforms under wet conditions but shows high noise levels during skin stretching and forearm waving, which might be attributed to electrode detachment or slippage during dynamic movements. In comparison, the nanomesh electrode shows more stable ECG signals under dynamic changing conditions, which is due to the stable conformal contact of electrode-skin interface. Corresponding SNR values are shown in Figure 4D, indicating high-quality ECG signals with low-motion artifacts. Continuous ECG waveforms were also recorded by the nanomesh electrode at various exercising states, as shown in Supplementary Figure 27 and Figure 4E. Before exercise, the ECG signals demonstrated a heart rate of 78 bpm; 1 min after exercise, the signals exhibited increased amplitude and a higher heart rate of 125 bpm; and after a 20-min recovery, the heart rate restored to 91 bpm. The R-R intervals before and after exercise are depicted in Figure 4F, which shows the statistical dispersion of two adjacent intervals. The heart-rate variability (HRV) indices are depicted in Supplementary Table 2. The SD1 and SD2 decreased immediately after exercise and recovered after resting, which is consistent with the sympathetic-parasympathetic modulation. The SD1/SD2 ratio dropped markedly after exercise (indicating sympathetic dominance) and returned to near-baseline levels after 20 min, suggesting a gradual restoration of autonomic balance.

High-quality EOG and EEG monitoring using the air-gap-free nanomesh electrode

EOG emerged as a valuable source of bioelectric signals, capable of reflecting both ocular movements and retinal electrical activity. EOG signals could be acquired by placing nanomesh electrodes above the eyebrow and on the lower orbital edge for recording; the experimental setup is illustrated in Figure 5A. Figure 5B presents the EOG recordings obtained under different ocular actions, including closed eyes, open eyes, blinking, upward gaze, and downward gaze. Different ocular actions can be distinguished by the EOG signals acquired from nanomesh electrode, indicating the applications in the fields of eye fatigue assessment and the human-machine interface.

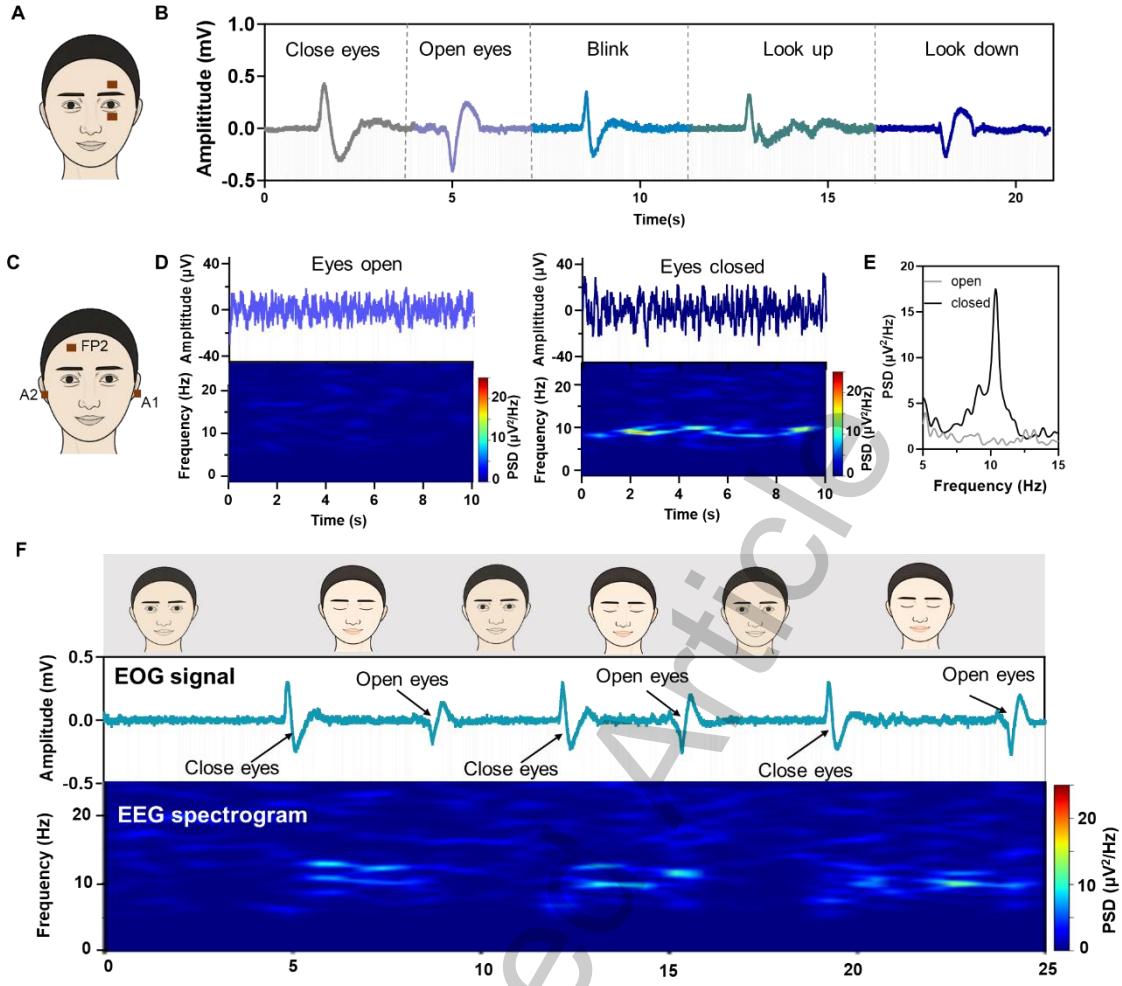

Figure 5. High-quality EOG and EEG monitoring using the air-gap-free nanomesh electrode. (A) Schematic of the experimental configuration for EOG monitoring with nanomesh electrode. (B) EOG signals recorded during various ocular activities. (C) Schematic illustration of EEG measurement setup using the nanomesh electrode. (D) EEG signals recorded during eyes-open and eyes-closed states, and corresponding spectrogram for α rhythms analysis. (E) PSD analysis of EEG signals during eyes-open and eyes-closed states. (F) EOG signals and EEG spectrogram during the eye-opening-closing cycle.

EEG signals originate from electrical activity of cerebral cortex, providing indispensable information for cognitive research, disease diagnosis, and neural feedback[46]. However, noninvasive EEG acquisition remains challenging because of the low amplitude of signals (μV scale), and the nanomesh electrode offers distinct advantages due to the high SNR[30]. For high-fidelity EEG monitoring, a three-electrode configuration was

employed [Figure 5C], with electrodes positioned on the right forehead (Fp2), right mastoid (A2), and left mastoid (A1) of a participant. After fast Fourier transformation treatment, the brain waves were categorized as follows: δ wave of 0.5-4 Hz, θ wave of 4-8 Hz, α wave of 8-13 Hz, and β wave of 10-30 Hz [Supplementary Figure 28]. Figure 5D compares the EEG activity between eyes-open and eyes-closed conditions, revealing higher signal amplitude with eyes closed. Moreover, the eyes-closed segment shows a pronounced high-power band centered around 8-12 Hz, corresponding to the α rhythm. Power spectral density (PSD) analysis in Figure 5E further reveals a distinct peak at 10 Hz in the eye-closed state, confirming the visual suppression of α activity when eyes are opened. Furthermore, the EOG and EEG signals are synchronously recorded during an eye-opening-closing cycle [Figure 5F], demonstrating the capability of nanomesh electrode for high-quality EOG and EEG measurement.

CONCLUSIONS

In summary, we introduce an ethanol-triggered interfacial reconstruction strategy to address the interfacial instability of dry epidermal electrophysiological electrodes. The proposed in situ approach eliminates interfacial air gaps, reduces mechanical mismatch, and establishes a seamless, stable, conformal, low-impedance nanomesh electrode directly on human skin for electrophysiological recordings. The resulting nanomesh electrode further integrates high breathability, sweat resistance, skin-friendly adhesion, and ethanol-assisted removability, allowing long-term, irritation-free wear with stable electrical performance under dynamic deformation. The nanomesh electrode achieves high-quality, motion artifact-resistant electrophysiological recordings of EMG, ECG, EOG, and EEG. This work establishes interfacial reconstruction as a route to construct epidermal bioelectronics for next-generation skin-interfaced bioelectronics in health monitoring, disease diagnosis, and brain-computer interfaces.

DECLARATIONS

Authors' contributions

Conceptualization, investigation methodology and data analysis: Huijun Kong, Chenshu Wu, Zhongqian Song

Data resources: Cuiyu Liu, Chenshu Wu, Weiyan Li

Administrative and technical support: Huijun Kong, Zhongqian Song, Li Niu

Writing and original draft: Huijun Kong

Funding, review and editing: Li Niu, Zhongqian Song

Availability of data and materials

All data are included in the main text or Supplementary Materials. Additional details are available from the corresponding authors upon request.

AI and AI-assisted tools statement

Not applicable.

Financial support and sponsorship

This work was supported by the National Natural Science Foundation of China (22404102, 22434007, 22104021, 52303075), the Taishan Young Scholar Program of Shandong Province (No. tsqnz20231235), Natural Science Foundation of Shandong Province (No. ZR2024QB338, ZR2023QB227), and the Medical and Health Technology Program of Shandong Province (No. 202525021304). Higher Education Institutions Youth Innovation Team Plan of Shandong Province (2024KJH046, 2024KJN011).

Conflicts of interest

All authors declared that there are no conflicts of interest.

Ethical approval and consent to participate

This study was limited to non-invasive electrical activity monitoring of on the surface of human skin, which caused no risk or discomfort to the participants. According to Article 32 of the "Measures for the Ethical Review of Life Science and Medical Research Involving Human Subjects (Trial)", this study meets the criteria for exemption from ethical review. The collection of electrophysiological data from human subjects was carried out with the consent of the volunteer.

Consent for publication

Not applicable.

REFERENCES

1. Wu, H.; Yang, G.; Zhu, K.; Liu, S.; Guo, W.; Jiang, Z.; Li, Z., Materials, Devices, and Systems of On-Skin Electrodes for Electrophysiological Monitoring and Human–Machine Interfaces. *Adv. Sci.* **2020,** *8* (2).DOI: 10.1002/advs.202001938

2. Wang, C.; He, K.; Li, J.; Chen, X., Conformal electrodes for on-skin digitalization. *SmartMat* **2021,** *2* (3), 252-262.DOI: 10.1002/smm2.1068

3. Wang, J.; Zhai, B.; Zhang, J.; Ning, H.; He, Q.; Wu, T.; Li, K.; Zhang, C.; Luo, Y.; Chi, A.; Ren, W.; Liu, Z.; Fang, Y., Stretchable, Breathable and Skin-conformal Nanofilm-based Epidermal Dry Electrodes for Electrophysiological and Motion Monitoring. *Adv. Funct. Mater.* **2026**, e24980.DOI: 10.1002/adfm.202524980

4. Zhu, M.; Wang, H.; Li, S.; Liang, X.; Zhang, M.; Dai, X.; Zhang, Y., Flexible Electrodes for In Vivo and In Vitro Electrophysiological Signal Recording. *Adv, Healthc. Mater,* **2021,** *10* (17), 2100646.DOI: 10.1002/adhm.202100646

5. Yan, W.; Liu, Y.; Wang, Y.; Yi, J.; Yang, J.; Wang, Z.; Sun, Q.; Zhou, P.; Zheng, M.; Huo, J.; Wang, Y., Conformal, Substrate-Free Liquid Metal Electrode for Continuous Health Monitoring. *ACS Sensors* **2025,** *10* (5), 3450-3460.DOI: 10.1021/acssensors.4c03449

6. Gogurla, N.; Kim, Y.; Cho, S.; Kim, J.; Kim, S., Multifunctional and Ultrathin Electronic Tattoo for On-Skin Diagnostic and Therapeutic Applications. *Adv. Mater.* **2021,** *33* (24), 2008308.DOI: 10.1002/adma.202008308

7. Zhao, Y.; Zhang, S.; Yu, T.; Zhang, Y.; Ye, G.; Cui, H.; He, C.; Jiang, W.; Zhai, Y.; Lu, C.; Gu, X.; Liu, N., Ultra-conformal skin electrodes with synergistically enhanced conductivity for long-time and low-motion artifact epidermal electrophysiology. *Nat. Commun.* **2021,** *12* (1), 4880.DOI: 10.1038/s41467-021-25152-y

8. Rauf, S.; Bilal, R. M.; Li, J.; Vaseem, M.; Ahmad, A. N.; Shamim, A., Fully Screen-Printed and Gentle-to-Skin Wet ECG Electrodes with Compact Wireless Readout for Cardiac Diagnosis and Remote Monitoring. *ACS Nano* **2024,** *18* (14), 10074-10087.DOI: 10.1021/acsnano.3c12477

9. Yang, S.; Jiang, X., Nanoscale Strategies for Enhancing the Performance of Adhesive Dry Electrodes for the Skin. *ACS Nano* **2024,** *18* (40), 27107-27125.DOI: 10.1021/acsnano.4c09477

10. Zheng, B.; Zhou, H.; Wang, Z.; Gao, Y.; Zhao, G.; Zhang, H.; Jin, X.; Liu, H.; Qin, Z.; Chen, W.; Ma, A.; Zhao, W.; Wu, Y., Fishing Net-Inspired Mutiscale Ionic

Organohydrogels with Outstanding Mechanical Robustness for Flexible Electronic Devices. *Adv. Funct. Mater.* **2023,** *33* (28), 2213501.DOI: 10.1002/adfm.202213501

11. Ye, H.; Wu, B.; Sun, S.; Wu, P., Self-compliant ionic skin by leveraging hierarchical hydrogen bond association. *Nat. Commun.* **2024,** *15* (1), 885.DOI: 10.1038/s41467-024-45079-4

12. Ma, J.; Feng, J.; Sa, Z.; Meng, F.; Feng, Z.; Sun, Q.; Sun, Y.; Wen, J.; Wang, S.; Tian, Y., High-precision electrohydrodynamic printing of EGaIn-AgNPs biphasic conductive ink for conformal and lightweight bioelectrodes. *Soft Sci* **2025,** *5* (4), 50.DOI: 10.20517/ss.2025.41

13. Yin, J.; Wang, S.; Tat, T.; Chen, J., Motion artefact management for soft bioelectronics. *Nat. Rev. Bioeng.* **2024,** *2* (7), 541-558.DOI: 10.1038/s44222-024-00175-4

14. Dong, J.; Liu, H.; Lim, T.; Oh, B.; Peng, Y.; Liu, T.; Park, S.; Huang, Y., Viscoelastic Adhesive, Super-Conformable, and Semi-Flowable Liquid Metal Eutectogels for High-Fidelity Electrophysiological Monitoring. *ACS Appl. Mater. Interfaces* **2024,** *16* (27), 34732-34742.DOI: 10.1021/acsami.4c06728

15. Yu, W.; Hao, S.; Zhang, G.; Hu, Z.; Jin, R.; Xu, X.; Cai, J.; Yang, J.; Shao, C.; Zhang, N.; Bai, Y., Autonomous In Situ Biointerfacing Platform for Real-Time Electrophysiological Monitoring and Advanced Wound Management. *ACS Nano* **2026,** *20* (7), 5764-5780.DOI: 10.1021/acsnano.5c17466

16. Zongman Zhang; Jiawei Yang; Haoyang Wang; Chunya Wang; Yuheng Gu; Yumiao Xu; Sunghoon Lee; Tomoyuki Yokota; Hossam Haick; Takao Someya; Wang, Y., A 10-micrometer- thick nanomesh- reinforced gas- permeable hydrogel skin sensor for long-term electrophysiological monitoring. *Sci. Adv.* **2024,** *10*, eadj5389.DOI: 10.1126/sciadv.adj5389

17. Yuli Wang; Zonglei Wang; Yujie Zhang; Jiawei Yang; Zongman Zhang; Pengcheng Zhou; Yumiao Xu; Qingyuan Sun; Meiqiong Zheng; Wenqing Yan; Xuezhong He; Jiongyu Chen; Juan Li; Youhua Jiang; Sunghoon Lee; Hossam Haick; Tomoyuki Yokota; Takao Someya; Wang, Y., A 2.7- μm- thick robust, permeable, and antifreezing hydrogel electrode for long- term ambulatory health monitoring. *Sci. Adv.* **2025,** *11*, eadt2286.DOI: 10.1126/sciadv.adt2286

18. Cheng, S.; Lou, Z.; Zhang, L.; Guo, H.; Wang, Z.; Guo, C.; Fukuda, K.; Ma, S.; Wang, G.; Someya, T.; Cheng, H. M.; Xu, X., Ultrathin Hydrogel Films toward Breathable Skin-Integrated Electronics. *Adv. Mater.* **2022,** *35* (1), 2206793.DOI:

10.1002/adma.202206793

19. Chunya Wang; Haoyang Wang; Binghao Wang; Hiroo Miyata; Yan Wang; Md Osman Goni Nayeem; Jae Joon Kim; Sunghoon Lee; Tomoyuki Yokota; Hiroshi Onodera; Someya, T., On-skin paintable biogel for long-term high-fidelity electroencephalogram recordin. *Sci. Adv.* **2022,** *8*, eabo1396.DOI: 10.1126/sciadv.abo1396

20. Li, L.; Ye, X.; Ji, Z.; Zheng, M.; Lin, S.; Wang, M.; Yang, J.; Zhou, P.; Zhang, Z.; Wang, B.; Wang, H.; Wang, Y., Paintable, Fast Gelation, Highly Adhesive Hydrogels for High-fidelity Electrophysiological Monitoring Wirelessly. *Small* **2025,** *21* (8), 2407996.DOI: 10.1002/smll.202407996

21. Lim, C.; Lee, S.; Kang, H.; Cho, Y. S.; Yeom, D.-H.; Sunwoo, S.-H.; Park, C.; Nam, S.; Kim, J. H.; Lee, S.-P.; Kim, D.-H.; Hyeon, T., Highly Conductive and Stretchable Hydrogel Nanocomposite Using Whiskered Gold Nanosheets for Soft Bioelectronics. *Adv. Mater.* **2024,** *36* (39), 2407931.DOI: 10.1002/adma.202407931

22. Ma, N.; Chen, Y.; Wang, L.; Tan, P.; Chen, N.; Jin, Y.; Song, J.; Li, G., Ag/AgCl@agar/P(AM-co-HEAA) hydrogel with ultra-stretchability, fatigue resistance, and freezing tolerance for human motion and electrophysiological signal monitoring. *Int. J. Biol. Macromol.* **2025,** *331*, 148239.DOI: https://doi.org/10.1016/j.ijbiomac.2025.148239

23. Chen, Y.; Guo, W.; Chen, N.; Liu, Y.; Wan, X.; Wang, T.; Zhou, Z.; Jin, Y.; Li, G., Skin-inspired MXene-based polyvinyl alcohol/gelatin organic hydrogel with good anti-drying, anti-swelling properties and high sensitivity. *SENSOR ACTUAT A-PHYS* **2025,** *383*, 116231.DOI: https://doi.org/10.1016/j.sna.2025.116231

24. Alsharif, A. A.; Milan Cucuri, N. S.; Mishra, R. B.; El-Atab, N., 3D Printed Dry Electrodes for Electrophysiological Signal Monitoring: A Review. *Adv. Mater. Technol.* **2023,** *8* (7), 2201677.DOI: 10.1002/admt.202201677

25. Jeon, M. S.; Yi, J.; Hong, S.; Lee, J.; Jang, H.; Kim, B.; Lee, H.; Lee, C. H.; Kim, D. R., All-Dry Self-Adhesive Soft Electrodes with Subsurface Pores for Long-Term Skin Recording. *Small* **2025,** *21* (49), e07416.DOI: 10.1002/smll.202507416

26. He, K.; Cai, P.; Ji, S.; Tang, Z.; Fang, Z.; Li, W.; Yu, J.; Su, J.; Luo, Y.; Zhang, F.; Wang, T.; Wang, M.; Wan, C.; Pan, L.; Ji, B.; Li, D.; Chen, X., An Antidehydration Hydrogel Based on Zwitterionic Oligomers for Bioelectronic Interfacing. *Adv. Mater.* **2024,** *36* (8), 2311255.DOI: 10.1002/adma.202311255

27. Ding, L.; Hang, C.; Yang, S.; Qi, J.; Dong, R.; Zhang, Y.; Sun, H.; Jiang, X., In Situ Deposition of Skin-Adhesive Liquid Metal Particles with Robust Wear Resistance for

Epidermal Electronics. *Nano Lett.* **2022,** *22* (11), 4482-4490.DOI: 10.1021/acs.nanolett.2c01270

28. International Journal of Biological MacromoleculesInternational Journal of Biological MacromoleculesLiu, X.; Wan, C.; Liu, J.; Xu, H.; Liu, Y.; Liu, Y.; Liu, Y.; Liu, J.; Wang, H.; Fan, H.; Guo, R., Liquid metal-based dynamic conformal electrodes. *Soft Sci* **2025,** *5* (3).DOI: 10.20517/ss.2025.16

29. Qiu, J.; Yu, T.; Zhang, W.; Zhao, Z.; Zhang, Y.; Ye, G.; Zhao, Y.; Du, X.; Liu, X.; Yang, L.; Zhang, L.; Qi, S.; Tan, Q.; Guo, X.; Li, G.; Guo, S.; Sun, H.; Wei, D.; Liu, N., A Bioinspired, Durable, and Nondisposable Transparent Graphene Skin Electrode for Electrophysiological Signal Detection. *ACS Mater. Lett.* **2020,** *2* (8), 999-1007.DOI: 10.1021/acsmaterialslett.0c00203

30. Du, X.; Yang, L.; Shi, X.; Ye, C.; Wang, Y.; Song, D.; Xiong, W.; Gu, X.; Lu, C.; Liu, N., Ultrathin Bioelectrode Array with Improved Electrochemical Performance for Electrophysiological Sensing and Modulation. *ACS Nano* **2024,** *18* (51), 34971-34985.DOI: 10.1021/acsnano.4c13325

31. Wang, J.; Zhou, Q.; Wang, A.; Zhu, Z.; Moses, K.; Wang, T.; Li, P.; Huang, W., Sponge Inspired Flexible, Antibacterial Aerogel Electrode with Long-Term High-Quality Electrophysiological Signal Recording for Human-Machine Interface. *Adv. Funct. Mater.* **2024,** *34* (23), 2309704.DOI: 10.1002/adfm.202309704

32. Fan, L.; Gao, F.; Xu, L.; Xun, X.; Zhao, S.; Yang, B.; Bi, H.; Zhao, X.; Liao, Q.; Zhang, Y., Electrochemically Enhanced Low-Impedance Ti3C2Tx MXene Epidermal Electrodes for Accurate Electrophysiological Monitoring. *Nano-Micro Lett.* **2026,** *18* (1), 297.DOI: 10.1007/s40820-026-02132-9

33. Zhang, L.; Kumar, K. S.; He, H.; Cai, C. J.; He, X.; Gao, H.; Yue, S.; Li, C.; Seet, R. C.-S.; Ren, H.; Ouyang, J., Fully organic compliant dry electrodes self-adhesive to skin for long-term motion-robust epidermal biopotential monitoring. *Nat. Commun.* **2020,** *11* (1).DOI: 10.1038/s41467-020-18503-8

34. Hwang, C.; Choi, J. G.; Pang, C.; Kim, M. S.; Park, S., Skin-Conformal Ag Flake-Decorated PEDOT:PSS Sensor Arrays for Spatially Resolved Body Temperature Monitoring. *Small* **2025,** *21* (32).DOI: 10.1002/smll.202412675

35. Hou, S.; Fan, X.; Jin, T.; Li, H.; Han, Y., A Highly Conductive, Stretchable, and Healable Sensing Electrode Consisting of PEDOT Conductive Pathway and Semi-Interpenetrating Network. *Adv. Funct. Mater.* **2026,** *36* (18), e19643.DOI: 10.1002/adfm.202519643

36. Yu, J.; Wan, R.; Tian, F.; Cao, J.; Wang, W.; Liu, Q.; Yang, H.; Liu, J.; Liu, X.; Lin, T.; Xu, J.; Lu, B., 3D Printing of Robust High-Performance Conducting Polymer Hydrogel-Based Electrical Bioadhesive Interface for Soft Bioelectronics. *Small* **2023,** *20* (19), 2308778.DOI: 10.1002/smll.202308778

37. Shin, J. H.; Choi, J. Y.; June, K.; Choi, H.; Kim, T. i., Polymeric Conductive Adhesive-Based Ultrathin Epidermal Electrodes for Long-Term Monitoring of Electrophysiological Signals. *Adv. Mater.* **2024,** *36*, 2313157.DOI: 10.1002/adma.202313157

38. Ma, C.; Hao, S.; Yu, W.; Liu, X.; Wang, Y.; Wang, Y.; Zhao, J.; Zhang, N.; Bai, Y.; Xu, F.; Yang, J., Compliant and breathable electrospun epidermal electrode towards artifact-free electrophysiological monitoring. *Chem. Eng. J.* **2024,** *490*, 151118.DOI: 10.1016/j.cej.2024.151118

39. Tian, Q.; Zhao, H.; Wang, X.; Jiang, Y.; Zhu, M.; Yelemulati, H.; Xie, R.; Li, Q.; Su, R.; Cao, Z.; Jiang, N.; Huang, J.; Li, G.; Chen, S.; Chen, X.; Liu, Z., Hairy-Skin-Adaptive Viscoelastic Dry Electrodes for Long-Term Electrophysiological Monitoring. *Adv. Mater.* **2023,** *35* (30), 2211236.DOI: 10.1002/adma.202211236

40. Gao, Y.; Li, B.; Zhang, L.; Zhang, X.; Xin, X.; Xie, S.; Lee, R. A.; Li, K.; Zhao, W.; Cheng, H., Ultraconformal Skin-Interfaced Sensing Platform for Motion Artifact-Free Monitoring. *ACS Appl. Mater. Interfaces* **2024,** *16* (21), 27952-27960.DOI: 10.1021/acsami.4c04357

41. Kim, J.; Park, S.; Jeon, J.; Kang, D.-h.; Bryan, G. M.; Broderick, T. J.; Stone, M.; Tsukruk, V. V., Robust Skin-Conformal Nano-Electrodes for Sustainable Health and Performance Monitoring. *ACS Nano* **2025,** *19* (33), 30322-30337.DOI: 10.1021/acsnano.5c08540

42. Zheng, Y.; Li, Y.; Zhao, Y.; Lin, X.; Luo, S.; Wang, Y.; Li, L.; Teng, C.; Wang, X.; Xue, G.; Zhou, D., Ultrathin and highly breathable electronic tattoo for sensing multiple signals imperceptibly on the skin. *Nano Energy* **2023,** *107*, 108092.DOI: 10.1016/j.nanoen.2022.108092

43. Mimuro, M.; Ebihara, Y.; Liang, X.; Inoue, D.; Hashizume, D.; Lee, S.; Yokota, T.; Yamagishi, K.; Someya, T., Breathable nanomesh electrodes with improved water resistance and stretchability for skin impedance monitoring. *npj flex. electron.* **2026,** *10* (1), 38.DOI: 10.1038/s41528-026-00542-8

44. Liu, T.; Nong, Z.; Li, Y.; Liu, Z.; Fan, Z.; Liu, H.; Liu, Q.; Qiu, J.; Wang, Q.; Liu, Z., Eutectogel Skin Electrodes with Superior Adhesion, Sweat Resistance, and Long-Term

Stability for Electrophysiological Signal Monitoring. *Adv. Funct. Mater.* **2025,** *35* (49), e03568.DOI: 10.1002/adfm.202503568

45. Zheng, S.; Du, M.; Miao, W.; Wang, D.; Zhu, Z.; Tian, Y.; Jiang, L., 2D Prior Spreading Inspired from Chinese Xuan Papers. *Adv. Funct. Mater.* **2018,** *28* (49), 1800832.DOI: 10.1002/adfm.201800832

46. Lin, S.; Jiang, J.; Huang, K.; Li, L.; He, X.; Du, P.; Wu, Y.; Liu, J.; Li, X.; Huang, Z.; Zhou, Z.; Yu, Y.; Gao, J.; Lei, M.; Wu, H., Advanced Electrode Technologies for Noninvasive Brain–Computer Interfaces. *ACS Nano* **2023,** *17* (24), 24487-24513.DOI: 10.1021/acsnano.3c06781